Supplement to: Observed large-scale trapping of gravity waves within the free troposphere

Giovanni Biagioli [1,★], **Alexis Aubel** [1,2,★], **Riwal Plougonven** [2], **and Sandrine Bony** [1]

[1]Laboratoire de Météorologie Dynamique/IPSL, Sorbonne Université, CNRS, Paris, France
[2]Laboratoire de Météorologie Dynamique/IPSL, École polytechnique, CNRS, Paris, France
★These authors contributed equally to this work.

Correspondence: Giovanni Biagioli (giovanni.biagioli@lmd.ipsl.fr)

1 Wave modulation of aerosol concentrations

We showed in Figure 3d that the PSD obtained from the FCDP probe exhibits a distinct, quasi-periodic modulation. The nature of the particles contributing to this signal requires careful evaluation as to whether it reflects in situ cloud formation or vertical transport of coarse-mode aerosol particles.

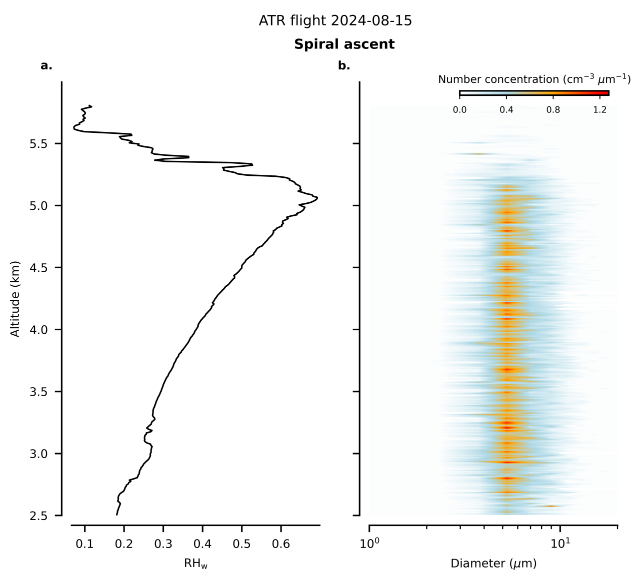

Figure S1. (a) Vertical profile of relative humidity with respect to liquid water and (b) FCDP-derived PSD as a function of particle diameter and altitude, during the aircraft spiral ascent through the Saharan Air Layer.

In situ formation of cloud particles in the cold phases of the wave seems unlikely, as relative humidity with respect to both liquid water and ice remains below saturation throughout the considered flight segment (Figure 3c) and condensational growth to micrometer-sized cloud particles cannot occur under subsaturated conditions. Instead, we argue that the observed signal is likely associated with wave-induced vertical displacements that modulate the concentrations of large mineral dust particles from the underlying SAL.

This interpretation is supported by measurements collected during the aircraft spiral ascent prior to the level flight leg in the mid-troposphere. The FCDP probe detects the presence of particles during most of the ascent and the corresponding profiles reveal that, within cloud-free Saharan air masses, particle concentrations and characteristic diameters are remarkably similar to those shown in Figure 3d, even where the relative humidity drops as low as 20-40% (Figure S1). This provides further evidence against the hypothesis of locally formed cloud condensate and suggests that the particles detected at 5.8 km are part of an ambient aerosol population. While at flight level water uptake by hygroscopic aerosol particles cannot be entirely ruled out, these observations appear overall consistent with the wave field modulating the coarse-mode aerosol population in the mid-troposphere.

2 Vertical profiles of the Richardson number on 15 August 2024

We showed in Figure A1c that, on 25 August 2024, the radiosonde-derived vertical profile of the gradient Richardson number falls below the critical threshold for shear-driven instability ($\mathrm{Ri}_c = 0.25$) at flight altitude. To investigate whether similar conditions occurred on 15 August, we computed the Richardson number from the aircraft and radiosonde vertical profiles closest in space and time to the

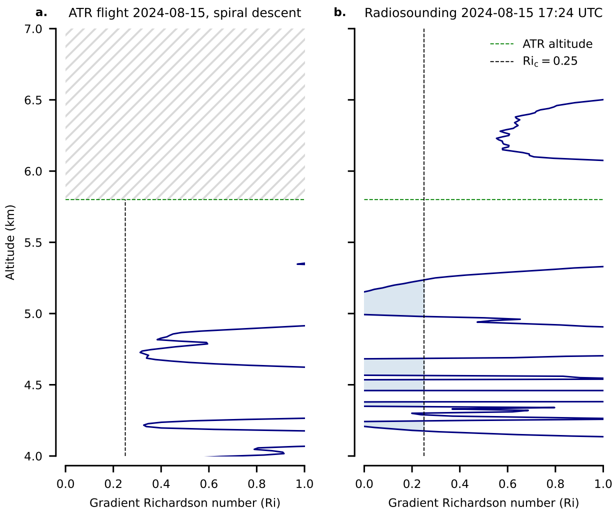

Figure S2. Vertical profiles of the gradient Richardson number computed from the aircraft spiral descent leg (a) and the closest radiosounding (b) on 15 August 2024 (see text for details). In both panels, the critical value $\mathrm{Ri}_c = 0.25$ for shear-driven instability is shown as a dashed black vertical line, while the flight altitude at the wave sampling location is represented as a dashed green horizontal line. In panel (a) the hatching indicates missing data above the maximum altitude reached by the aircraft.

wave sampling segment. In particular, regarding airborne data, the spiral descent was selected over the ascent based on this maximum spatiotemporal proximity criterion.

The corresponding Ri vertical profiles are shown in Figure S2. Contrary to the 25 August event, on 15 August both profiles are well above the critical threshold for shear-driven instability at and around flight level. We note that, in both cases, the Richardson number was computed by smoothing the vertical profiles of θ_v, u and v with a local least-squares third-order polynomial filter with a 500m vertical window. This removes the high-frequency noise before differentiation (see Eq. 2), while ensuring that physically meaningful vertical variations in Ri are accurately captured.

3 Model representation of large-scale conditions on 15 August 2024

To further confirm the spatiotemporal representativeness of the large-scale environmental conditions sampled by the 15 August radiosoundings and conducive to wave trapping (Section 3.4), we analyzed the output of high-resolution numerical simulations performed in parallel to the ORCESTRA campaign (Stevens et al., 2026).

Our analysis considers the cloud-resolving model AROME (Seity et al., 2011), which was run daily and provided forecasts up to four days ahead, over a domain (1° S – 25° N, 40° W – 10° W) that fully encompasses the Cape Verde islands. It was operated at 1.3 km horizontal resolution, with lateral and surface boundary conditions provided by the global operational model ARPEGE. Additionally, we evaluated the simulation output from the ICON model, run daily at 1.25 km horizontal resolution over a wide regional domain (4° S – 24° N, 64° W – 8° W). These ICON limited-area simulations were initialized with IFS analysis and run for 48 hours, forced by IFS forecasts, with the first 24 hours treated as a spin-up period (Fiévet et al., 2026).

Figure S3 shows the vertical profiles of potential temperature predicted by AROME at 17:00 UTC on 15 August 2024, sampled on a regular 1° × 1° grid within a 5° × 5° region that encompasses the Cape Verde islands. This figure shows a striking similarity with Figure 5a, particularly in the lower- to mid-troposphere, where the well-mixed Saharan Air Layer is clearly evident up to approximately 550 hPa. The analysis of ICON model output yielded similar results (not shown), providing further confidence in the ubiquity of these distinctive large-scale environmental conditions.

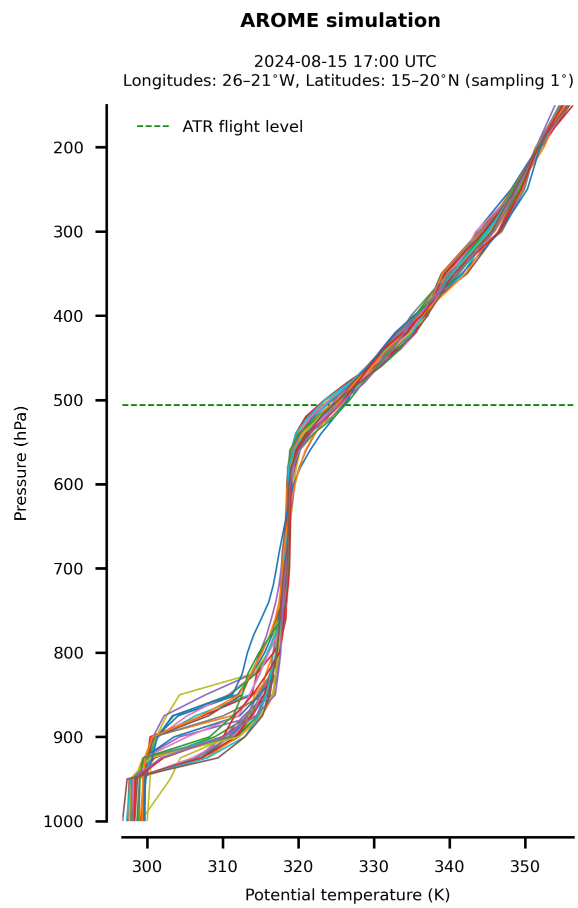

Figure S3. Vertical profiles of potential temperature over the region 26° W – 21° W, 15° N – 20° N sampled on a regular 1° × 1° grid, as predicted by the AROME model at 17:00 UTC on 15 August 2024. The dashed green horizontal line indicates the ATR flight level at the wave sampling location.

4 Further details on the idealized cavity model

4.1 Mode-specific hodographs

The Fourier decomposition of u' and w' (Figure 6) shows peaks that align well with the horizontal wavelengths of the trapped modes predicted by the idealized cavity model. To verify that the observed modes indeed belong to the same wave train, we constructed hodographs from the band-pass-filtered timeseries of (u', v'), using frequency bands corresponding to horizontal wavelengths within $\pm 10\%$ of the theoretical trapped mode wavelengths.

The results are presented in Figure S4, with the direction of horizontal phase propagation, $\phi = 125°$ (inferred in Section 3), shown as a dashed gray line. All modes except the first one display an elliptical polarization, with the major axis aligned with ϕ between approximately 17:18 and 17:23. The first mode, and all others in the early part of the transect, exhibit wave activity associated with a different propagation direction, aligned zonally (E-W). This secondary wave train cannot be responsible for the cloud stripes observed in Figure 1f, which are perpendicular to the 125° propagation direction and not oriented meridionally. Nevertheless, its trapped modes share common characteristic mode wavelengths with those identified in the main wave packet. This is consistent with the environmental filtering of the observed wave modes, further supporting the interpretation provided in Section 3.5. A detailed analysis of this secondary wave train, however, is beyond the scope of the present study, and is not explored further.

4.2 Possible extensions

The poly-chromatic cavity model introduced in Section 3.5 relies on three simplifying assumptions: (i) a stepwise constant stratification profile; (ii) the absence of background wind shear; (iii) infinitely deep evanescent layers at the waveguide boundaries. In this section, we discuss how more realistic atmospheric profiles would modify the wave propagation and mode selection.

Concerning (i), if a realistic, continuous vertical profile of N is considered, the vertical wavenumber becomes a function of altitude, $m = m(z)$. This induces a local vertical stretching or compression of the wave structure as it propagates through layers of varying stability, given by

$$\frac{\partial_z m}{m} = \frac{N \partial_z N}{N^2 - \hat{\omega}^2}.$$

Since this vertical stretching factor is independent of the horizontal wavenumber k, all wave modes are modulated in the exact same way. As the phase shift ψ upon reflection at the boundaries is also independent of k (Eq. 12), the geometric properties of the wave modes – specifically the vertical distribution of nodes and antinodes – are preserved, subject only to a vertical coordinate stretching. Finally, we note that, for the derivation of wave parameters, as a representative value of N, we chose its average between $5-8$ km altitude (Section 3.4), which is higher than the average over the full waveguide. Accounting for the weakening of $N(z)$ towards the boundaries yields smaller vertical wavenumbers (Eq. 11) and a larger phase shift upon reflection (since $\partial \psi / \partial N < 0$). Both effects require a deeper cavity to satisfy the resonance condition (13), consistent with the deeper waveguide observed in Figure 5e relative to the baseline choice of $H = 3.2$ km.

Concerning (ii), a realistic (sheared) wind profile $U = U(z)$ would introduce a Doppler shift, making the intrinsic frequency $\hat{\omega}$ dependent on altitude. However, if we assume a linear wind profile ($d^2U/dz^2 = 0$), the main effects of shear can be qualitatively absorbed into an effective, representative $N(z)$ profile, preserving the simplicity of our cavity model. A formal investigation of more complex wave-mean flow interactions is beyond the scope of this study.

Concerning (iii), in a realistic atmosphere, the neutral evanescent layers limiting the waveguide have a finite thickness h. Consequently, full reflection might not be achieved at the boundaries, and a fraction of the wave energy can leak through a mechanism analogous to quantum tunnel effect. This becomes significant when the vertical e-folding decay scale of the evanescent wave is comparable to or larger than the thickness of the layer, i.e., when $kh \leq 1$, or equivalently $\lambda_x \geq 2\pi h$. For instance, for $h \approx 3$ km, the tunnel effect would affect only modes with large horizontal wavelengths, $\lambda_x \geq 20$ km. This means that energy leakage is negligible for the small-scale GWs considered here (Figure 7). In any case, we remark that such a criterion highly selects the modes that can (or cannot) remain trapped inside a given waveguide.

5 Analysis of MAESTRO radiosoundings

We considered all available radiosoundings conducted during the MAESTRO campaign to characterize the large-scale environmental conditions over the Cape Verde region. In fact, while individual soundings are local, their composite effectively captures the variability of the tropical background state, strongly modulated by the passage of synoptic-scale disturbances (Winkler et al., 2026). This high-resolution observational dataset was used to validate our hypotheses on the leading-order mechanism of upper-level wave reflection and to evaluate the ability of TraLI to identify conditions conducive to wave trapping.

A systematic comparison of the vertical profiles highlights that, in the upper troposphere, the wind field exhibits a distinct transition towards the end of August 2024, shifting from a strong upper-tropospheric flow to a significantly weaker regime that persists through September (Figure S5b). In contrast, the upper-level stratification displays comparatively little variability over the same period (Figure S5a). This pronounced asymmetry supports our hypothesis, consistent with the findings of the case study: whenever upper-level wave re-

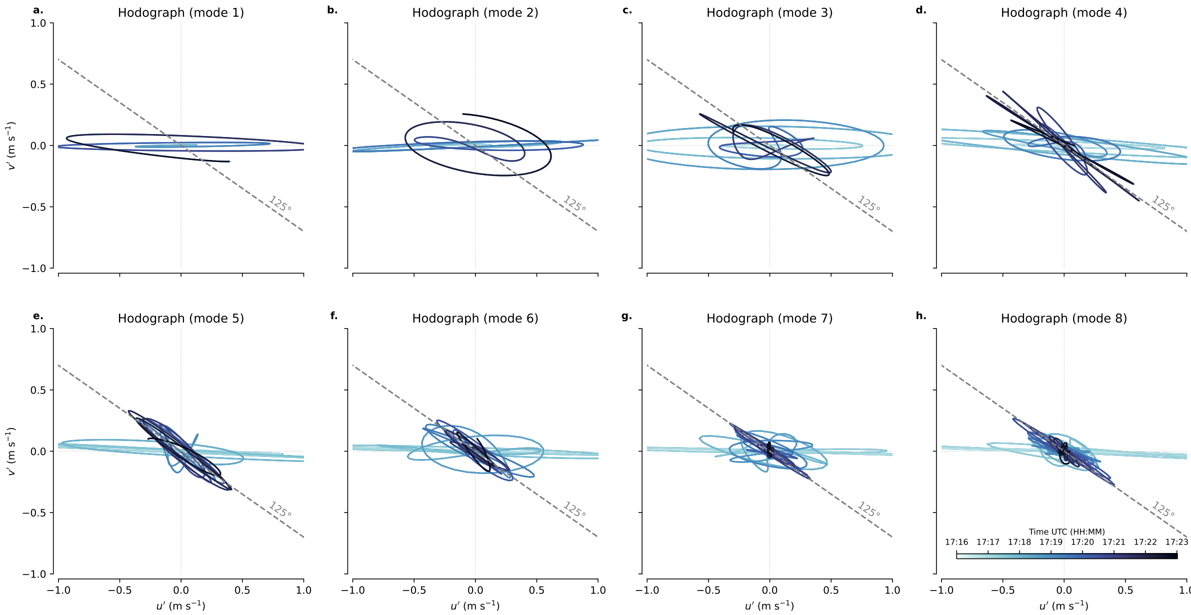

Figure S4. Mode-specific hodographs for the first eight modes of the idealized cavity model. Each panel was constructed as in Figure 4b, using band-pass-filtered timeseries of horizontal wind anomalies (u', v') (see text for details).

flection occurs, it is controlled primarily by the wind field rather than by variations in static stability. Conversely, the lower troposphere exhibits relatively weak variability in the wind field and more pronounced fluctuations in N^2, suggesting that the thermal structure is the leading-order control on the lower portion of the simplified Scorer parameter S_0 (Figure S5c).

The S_0 profiles are consistent with the time series shown in Figure 8. Specifically, periods characterized by elevated lower- and upper-TraLI values correspond well to periods when S_0 drops below the critical threshold S_c (indicated by the white contour in Figure S5c) in the lower and upper troposphere, respectively. In particular, between 10 and 15 August 2024, the large-scale environment appears favourable for free-tropospheric wave trapping, with $S_0 < S_c$ in both the lower and upper troposphere.

Finally, a comparison with the gradient Richardson number (Ri) highlights the advantage of our approach: while Ri vertical profiles are dominated by high-frequency noise (Figure S5d), S_0 constitutes a much cleaner diagnostic, with greater temporal and vertical coherence, thus enabling a more direct indication of environmental conditions conducive to waveguide formation and a more direct link to wave characteristics (through S_c).

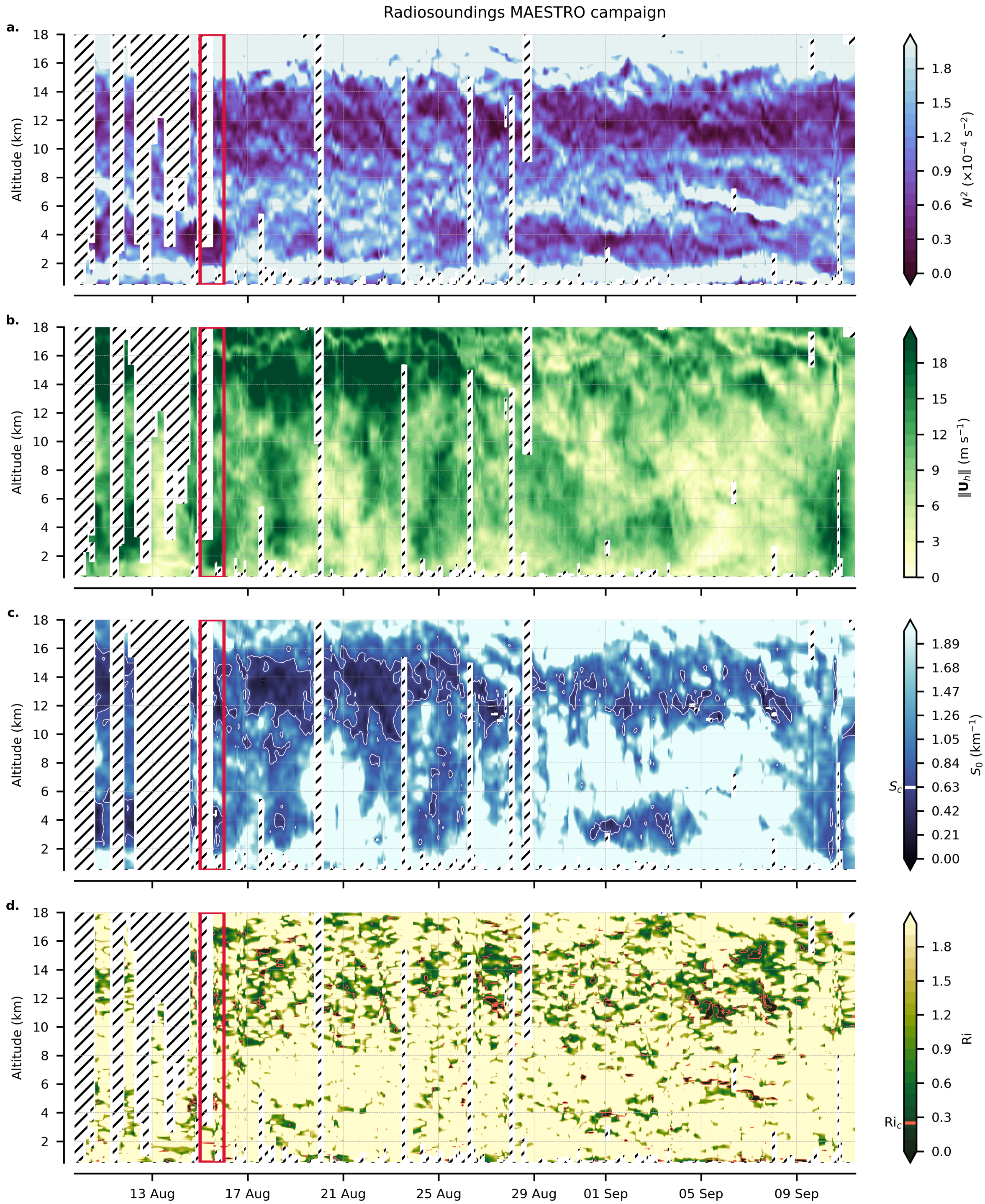

Figure S5. Time-height cross-sections of different variables from radiosondes launched at Sal island, including both ascent and descent profiles from each sounding: (a) squared Brunt-Väisälä frequency, N^2; (b) horizontal wind speed $\|\mathbf{U}_h\| = \sqrt{u^2+v^2}$, u and v being the zonal and meridional wind components; (c) simplified Scorer parameter, S_0 (Eq. 14); (d) gradient Richardson number, Ri (Eq. 2). The critical thresholds $S_c = 0.6$ km^{-1} and $\mathrm{Ri}_c = 0.25$ are shown as white and red contours in panels c and d, respectively. In all panels, hatched areas correspond to missing data, while the date of our selected case study (15 August 2024) is outlined by a red rectangle. All vertical profiles of u, v, potential temperature θ and virtual potential temperature θ_v were smoothed prior to the computation of N^2, S_0 and Ri using a local least-squares second-order polynomial filter with a 1 km smoothing window to reduce the impact of high-frequency noise on vertical derivatives.

References

Fiévet, R., Linardakis, L., Kornblueh, L., Daniel-Lacombe, M., Gloeckner, H., Fiolleau, T., Kluft, L., Hohenegger, C., and Stevens, B.: Tropical convection and storm-resolving modeling: a case study based on the ORCESTRA campaign, https://doi.org/10.22541/essoar.177315810.09022965/v1, 2026.

Seity, Y., Brousseau, P., Malardel, S., Hello, G., Bénard, P., Bouttier, F., Lac, C., and Masson, V.: The AROME-France Convective-Scale Operational Model, Monthly Weather Review, 139, 976 – 991, https://doi.org/10.1175/2010MWR3425.1, 2011.

Stevens, B., Bony, S., Gross, S., Klocke, D., Windmiller, J. M., Wing, A. A., von Bismarck, J., Brito, E., David, R. O., Delanoë, J., Farrell, D., and Wu, Y.: ORCESTRA: Organized Convection and EarthCARE Studies Over the Tropical Atlantic, Tellus, 79, 35–52, https://doi.org/10.16993/tellus.4123, 2026.

Winkler, M., Rixen, M., Beucher, F., Couvreux, F., Nam, C. C., Peyrillé, P., Schmidt, H., Segura, H., Wieners, K.-H., Alkilani-Brown, E., Coly, A. A., Biagioli, G., Bell, M. M., Brito, E., Chauvin, E., Capo, J., Colón-Burgos, D., Dawes, A., da Luz, J. C., Demiralay, Z., Douet, V., Ducastin, V., Dufaux, C., Dufresne, J.-L., Favot, F., Fiolleau, T., Fons, E., George, G., Gloeckner, H. M., Gonçalves, S., Gouttesoulard, L., Hayo, L., Hsiao, W.-T., Kennison, S., Kopelman, M., Lee, T.-Y., Le Gall, E., Lovato, M., Luschen, E., Maury, N., McKim, B., Netz, L., Ousseynou, D., Peters-von Gehlen, K., Pope, C., Poujol, B., Rivera Maldonado, N., Robbins-Blanch, N., Rochetin, N., Rowe, D., Romero Jure, P., Ruppert Jr., J. H., Segura Bermudez, J., Starr, J. C., Stelzner, M., Stoll, C., Syrett, M., Tekoe, A., Trules, J., Welty, C., Klocke, D., Vogel, R., Bony, S., Wing, A. A., and Stevens, B.: RAPSODI: radiosonde atmospheric profiles from ship and island platforms during ORCESTRA, collected to Decipher the ITCZ, Earth System Science Data, 18, 1833–1854, https://doi.org/10.5194/essd-18-1833-2026, 2026.